



Superefficient microcombs at the wafer level

Downloaded from: <https://research.chalmers.se>, 2025-07-03 15:55 UTC

Citation for the original published paper (version of record):

Girardi, M., Helgason, Ò., López Ortega, C. et al (2025). Superefficient microcombs at the wafer level. *Optics Express*, 33(13): 27451-27460. <http://dx.doi.org/10.1364/OE.563489>

N.B. When citing this work, cite the original published paper.



Superefficient microcombs at the wafer level

MARCELLO GIRARDI,¹  ÓSKAR B. HELGASON,¹  CARMEN H. LÓPEZ-ORTEGA,¹ ISRAEL REBOLLEDO-SALGADO,^{1,2}  AND VICTOR TORRES^{1,*} 

¹*Department of Microtechnology and Nanoscience, Chalmers University of Technology, Göteborg SE-41296, Sweden*

²*Measurement Science and Technology, RISE Research Institutes of Sweden, Borås SE-50115, Sweden*

**torresv@chalmers.se*

Abstract: Chip-scale frequency combs offer massive wavelength parallelization, holding a transformative potential in photonic system integration with potential application in future navigation systems, data center interconnects, and ranging. However, efficient frequency comb solutions have only been reported at the die level. Here, we report the wafer level characterization of soliton microcombs with an average conversion efficiency exceeding 50%, featuring 100 lines at 100 GHz repetition rate with 20 MHz standard deviation. We further illustrate the enabling possibilities of the space multiplicity, i.e., the large wafer-level redundancy, for establishing new sensing applications, and show tri-comb interferometry for broadband phase-sensitive spectroscopy.

Published by Optica Publishing Group under the terms of the [Creative Commons Attribution 4.0 License](https://creativecommons.org/licenses/by/4.0/). Further distribution of this work must maintain attribution to the author(s) and the published article's title, journal citation, and DOI.

1. Introduction

Photonic integrated circuits (PICs) are devices that process light on a chip by waveguiding [1]. Following the electronic industry footprints, photonic research is transferring an increasing number of functionalities to integrated platforms with the aim of implementing full photonic systems on a chip [2,3]. This is beneficial for the steady deployment of photonic integrated circuits in large-scale markets, such as transceivers for data center interconnects [4–7] and LiDARs [8–10] for automotive applications. These markets require mature integration platforms that can potentially supply millions of devices per year and provide efficient solutions in terms of power consumption, wavelength multiplicity, and optical performance [2].

Silicon is one of the most successful material platforms for photonic integration, with silicon-on-insulator (SOI) as the standard wafer available in sizes up to 300 mm. In the last two decades, this platform evolved from research to commercialization [11], and it has been deployed in communication transceivers modules since 2007 [12]. Silicon photonics developed widely thanks to its similarities with standard complementary metal-oxide semiconductor (CMOS) manufacturing, which kept the cost of PIC fabrication low and guaranteed the volume necessary for scalability in a consumer market. Meanwhile, other platforms such as silicon nitride [13,14], lithium niobate [15,16] and III-V materials [17] are being developed, and some are emerging at the commercial level [18,19] with prototype lines. These platforms benefit from the same economy of scale that established SOI as the de facto standard to build the next generation of PICs [20,21].

One of the recent milestones in PICs is the integration of narrow linewidth lasers [22] on a Si₃N₄ platform that displays ultra-low loss in the telecom frequency range. This achievement enables the development of photonic systems on a chip for applications such as spectroscopy [23], or coherent optical communications [24]. However, these applications require massive wavelength parallelization, which translates into the integration of tens to hundreds of lasers

on-chip. This large-scale multiplicity can be easily achieved with integrated microresonator frequency combs (microcombs) [25–27].

Dissipative Kerr soliton (DKS) microcombs rely on a $\chi^{(3)}$ nonlinear microcavity driven by a continuous-wave laser. Soliton pulses come out of the cavity at a rate commensurate to the free spectral range. The periodic sequence of the pulse train results, in the frequency domain, into a set of evenly spaced narrow lines underneath a smooth hyperbolic secant shape. The spectrum is so broad that hundreds of lines at ultrahigh (>100 GHz) repetition rates may be generated. Crucially, this is broader than other chip-scale comb technologies relying on semiconductor materials [28], and the repetition rate is higher than state-of-the-art low-noise RF oscillators needed in, e.g., electro-optic comb generators [29,30]. Soliton microcombs are generated all-optically, and the DC current used to control the cavities has in practice a negligible influence on the overall wall-plug efficiency. The efficiency of the comb generation process is crucial to maximize the optical power available on the PIC. Recently, efficient solutions have been reported in the literature [31–35] but they have only been demonstrated at the die level. To exploit the full potential of chip-scale comb generators for practical, large-volume applications, it is paramount to address their scalability.

Silicon nitride has been manufactured with ultralow-loss at the wafer-level before [14,19,36], but it remains unclear whether the process will result into high-performance reproducible microcombs in coupled cavities. Only reproducible designs that can tolerate the process variation in a standard CMOS line will be able to satisfy a market that requires millions of devices. For example, in wavelength division multiplexing (WDM) communications, line spacing differences between transmitter and receiver of 100 MHz will result into accumulated channel offset differences outside the intradyne bandwidth for carrier offset frequency estimation [37]. In the context of dual-comb spectroscopy [38], the ability to control the repetition rate difference between combs is crucial to map the optical frequency measurement range within the electronics bandwidth. Being unable to control these characteristics with high statistical accuracy at the wafer level will demand testing large sample sets, thus negating the economics of scale enabled by integrated optics.

Our fabrication relies on a subtractive manufacturing process where the Si_3N_4 is deposited on an oxidized Si wafer with 3 μm of SiO_2 . A large area is available on the wafer without any pre-patterned structures thanks to the crack barriers positioned on the perimeter (Fig. 1(a) and (b)). This provides high flexibility in the chip dimensions and the design of the devices combined with high fabrication yield.

In this work, we demonstrate that photonic molecule super-efficient microcombs [35] can be manufactured on a wafer scale with a fabrication yield of 98%. All the tested frequency combs display high power-conversion efficiency - the 25th percentile and the average are 50.3% and 50.7%. This is to the best of our knowledge the first statistical analysis of chip-scale frequency comb generators of any kind. These results not only represent a crucial step towards the large-scale deployment of chip-scale frequency combs in mass-market applications but also open new scientific opportunities. To display the enabling possibilities of the high reproducibility and yield, we realize tri-comb spectroscopy. Specifically, spectrally phase-sensitive signals over 40 nm bandwidth can be obtained in a highly parallel manner using a common local oscillator comb. Overall, these results represent a crucial step towards deploying microcomb technology in large-scale applications, where the CMOS processes can be exploited to fabricate millions of devices.

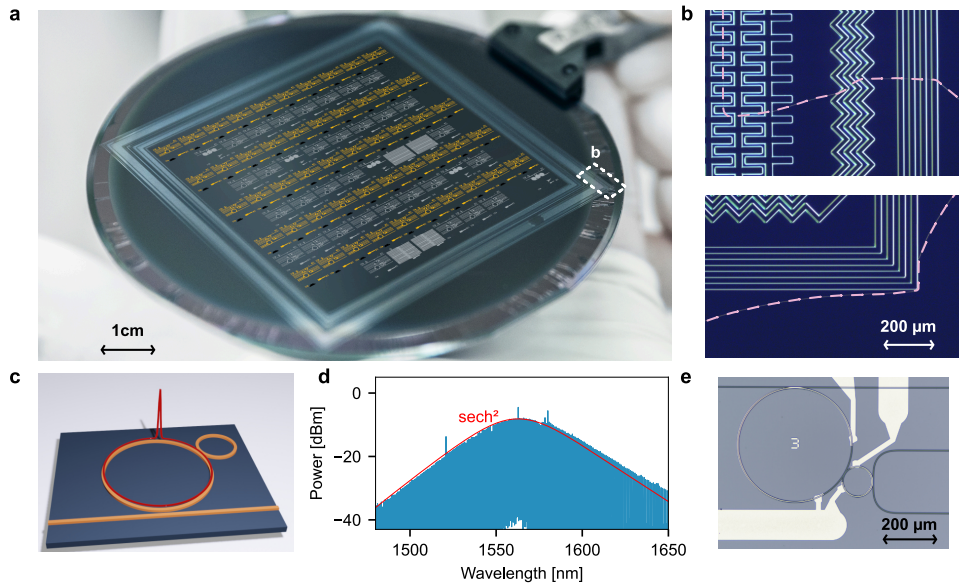


Fig. 1. Wafer-scale fabrication of soliton microcombs. (a) Picture of a wafer before the singulation process with crack barriers patterned at the edge of the chip area. The 50 chips measured in this work are highlighted in orange. 40 more chips that are not part of this work are present on the wafer (highlighted in white). (b) The design of the barrier defects (highlighted by the dashed violet line) avoiding propagation of the defects in the patterned area, allowing for the wafer-scale processing of ultra-low-loss silicon nitride PICs with high yield in strong optical confinement waveguide geometries. A dashed rectangle in (a) highlights the area represented in these pictures. (c) The soliton comb is generated in the main cavity with the auxiliary cavity introducing a constant phase shift of the pump mode. The shift enables an increased amount of pump power coupled in the main cavity, i.e., a higher power conversion efficiency. (d) One of the power-efficient frequency comb generated with the sech^2 envelop fitting. (e) Microscope picture of one of the devices with the main and auxiliary ring resonators and the metal heaters used to tune the cavities.

2. Wafer-level fabrication of microcombs

The generation of dissipative Kerr solitons requires a material that displays a balance between nonlinearities, anomalous group velocity dispersion (β_2), and low optical losses [26]. Si_3N_4 is an excellent platform that has been widely investigated to generate frequency combs in the near-infrared [39]. The generation of frequency combs on-chip requires careful dispersion engineering of the optical waveguide and in this study, we designed combs operating in the anomalous dispersion regime ($\beta_2 < 0$). The stoichiometric Si_3N_4 used in our fabrication process displays anomalous dispersion in the telecom C band (1550 nm) when the waveguide core has a thickness larger than 650 nm. However, the fabrication of Si_3N_4 films above 400 nm presents challenges in terms of crack management because of the high stress accumulated in the film during deposition [2,40,41]. Stress-generated cracks hinder fabrication with high yield, hence stress release patterns are necessary to stop the crack diffusion in the interested area of the wafer. These crack barriers consist in structures etched in the bottom cladding and in the Si substrate to dissipate the energy of the crack [42]. They can be as simple as scratches performed with a diamond tip [40], complex patterns surrounding the photonic devices [43,44], or diced at the edges of the interested area [41]. On our wafers, we etch the crack barrier at the perimeter of the patternable area of the wafer. This allows us to redesign the photonic layer after the material is

deposited. Our crack barriers are etched in the bottom cladding and provide a crack-free area of $56 \times 56 \text{ mm}^2$ on a 100 mm wafer (Fig. 1(a)). The cracks are efficiently stopped by the crack barriers, as shown in Fig. 1(b). We can easily accommodate 100 chips with size $5 \times 5 \text{ mm}^2$ in the crack-free area.

We fabricated ninety chips on the wafer, fifty of which are dedicated to studying the yield of power-efficient frequency combs. The chips are organized in five columns and ten rows, to cover the entire crack-free area, as displayed by the orange pattern highlighted in Fig. 1(a). Each chip included one device, where two ring resonators are coupled to generate a power-efficient comb, similar to [35]. A microscope picture of a representative device is reported in Fig. 1(e). The device consists of a main cavity, with a radius of $227.82 \text{ }\mu\text{m}$, and an auxiliary cavity with a radius of $60 \text{ }\mu\text{m}$. The waveguide width is $1.8 \text{ }\mu\text{m}$ for the bus coupler, the main cavity, and the auxiliary cavity. The two resonators are designed to have a free spectral range close to 100 GHz and 380 GHz respectively. The input and output of the chip have spot-size converters designed to couple to a lensed fiber with a mode field diameter of $2.5 \text{ }\mu\text{m}$. In Fig. 1(d) we report one of the combs generated with the expected sech^2 fitted curve. The strong attenuation of the pump is due to the high conversion efficiency; it showcases the potential of this type of frequency comb, where the pump does not need to be filtered out.

The deposition of Si_3N_4 via low-pressure chemical vapor deposition yields an inhomogeneous thickness on the wafer [45]. On our wafer, the thickness variation is 2.4% across the wafer and 1.4% within the crack barriers. This variation affects the core geometry of the waveguides fabricated in different areas of the chip, hence it modifies the dispersion. This can have a great impact on the performance of the frequency comb, as we will discuss in the frequency comb generation section. In a research environment, the design of every chip can be tailored to the local thickness of the material, but this might be not acceptable in large-scale manufacturing. To demonstrate that the power-efficient soliton generation is tolerant to variation in the fabrication parameters, we replicate the same design on every chip.

3. Linear characterization

To assess the fabrication yield we started with the linear characterization of the devices. We assessed the optical loss, the free spectral range (FSR), and group velocity dispersion (β_2) via swept wavelength interferometry [46] (see details in Supplement 1). In Fig. 2(f), we report the histogram of the intrinsic linewidth ($\kappa_0/2\pi$) for the processed resonances of all the devices measured, corresponding to over 9000 resonances. The most probable value is 13.5 MHz which corresponds to a quality factor of 14.2×10^6 and an equivalent propagation loss of 2.6 dB/m. The fabrication yield is 98%, with a single chip failure due to residual particles on the bus waveguide. The chip in question is on the bottom left side of the pattern, as illustrated by the red marker (*) in Fig. 2(b), where we report the distribution of the linewidth and the β_2 across the wafer. Each value is the average of two adjacent chips on the same column. As expected, the β_2 value changes across the wafer and it is higher in the center, where the Si_3N_4 thickness is lower. This is also illustrated in the map in Supplement 1 Fig. S1c, where we report the β_2 value of every device. The histograms in Fig. 2(g) and 2(h) show the distributions of the FSR and β_2 values respectively. With a mode solver simulation, we calculated the expected parameters for this waveguide geometry and we obtained that the most probable value of the FSR and β_2 are respectively 99.7 GHz and $-72 \text{ ps}^2/\text{km}$, in line with the experimental results. This analysis illustrates the ability to perform accurate designs of ultra-high-Q resonators with our silicon nitride process.

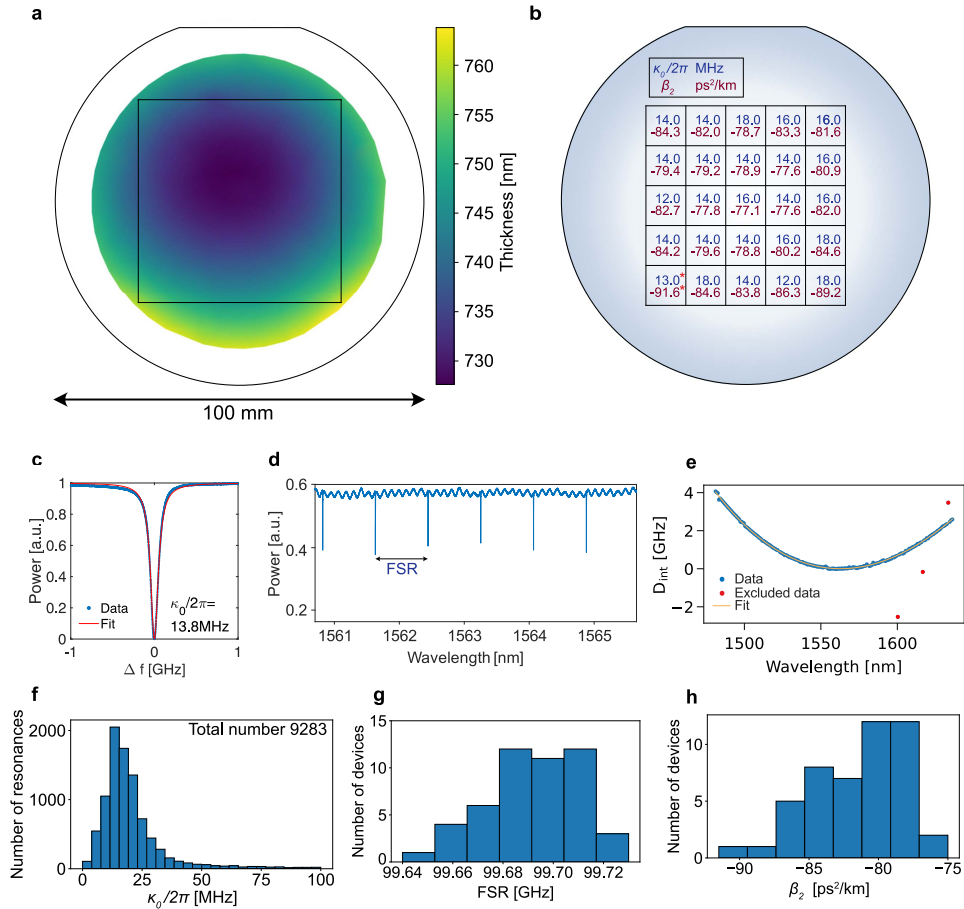


Fig. 2. Linear characterization of the coupled ring resonators. (a) Thickness map of the Si_3N_4 layer deposited via low-pressure chemical vapor deposition with the outline of the wafer (circle) and the area dedicated to chip fabrication (square). (b) Uniformity analysis on the 100 mm wafer. The most probable value of the intrinsic linewidth $\kappa_0/2\pi$ and measured group velocity dispersion β_2 are reported as the mean between two adjacent chips. The red asterisk marks the cell with the faulty chip. (c) Representative resonance of the main cavity and the fitted resonance shape. (d) Portion of the transmission spectrum of one of the devices measured displaying the FSR. The background oscillation corresponds to the Fabry-Perot cavity formed by the reflections at the chip facets. (e) Typical plot of the integrated dispersion, with highlighted in red the points excluded due to the interaction with the auxiliary cavity. (f) Histogram of the intrinsic linewidth $\kappa_0/2\pi$ of all the resonances measured on the wafers. (g), (h) Histograms of the free spectral range and the group velocity dispersion of the main cavity.

4. Frequency comb generation

After the linear characterization of the devices, we generated a frequency comb in each device. In Fig. 3(a) we report the 49 combs generated with power conversion efficiency ranging between 24 and 63%. The color of the comb represents the conversion efficiency, as displayed in the color bar on the right of the plot. The power conversion efficiency is on average 50.7% and the 25th percentile is 50.3%. Indeed, the majority of the devices display a conversion efficiency greater than 50% with the most probable value at 53.7%, as seen in Fig. 3(b). To the best of our

knowledge, the maximum conversion efficiency of 63% obtained in these measurements is the highest conversion efficiency recorded in a single DKS driven by a continuous-wave laser. We follow a similar procedure to generate the frequency combs as in Ref. [35], and detailed in the Supplement 1. Briefly, the laser frequency is tuned to the frequency doublet that arises from the coupling between cavities. A proportional-integral-derivative (PID) closed control loop is configured [47], acting on the laser to maintain a set power value. Afterwards, the set voltage on the auxiliary heater is changed to trigger the formation of a single soliton. Once the formation is confirmed, the pump power is reduced until a high-conversion efficiency is maintained. This process (Fig. 3(d)) is highly repeatable and can potentially be automated with the aid of an field-programmable gate array, underpinning the scalability of the characterization process.

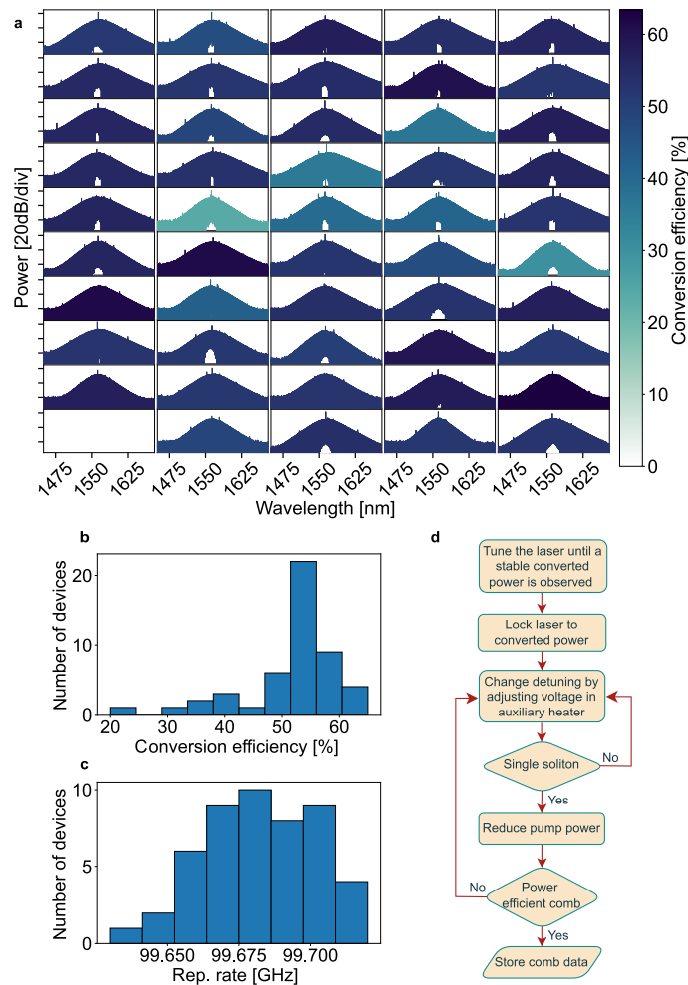


Fig. 3. High yield generation of power-efficient microcombs. (a) Spectra of every soliton comb generated across the wafer. The color of the plot represents the power conversion efficiency of the soliton. (b), (c) Histograms of the power conversion efficiency and the repetition rate of the generated soliton comb. (d) Block diagram of the algorithm used to obtain the highest conversion efficiency in each device reported in this work.

The power conversion efficiency is influenced by multiple factors. $\kappa_0/2\pi$, β_2 , and coupling between cavities ($\kappa_{aux}/2\pi$) are presented in the plots in Fig. S2a-c. We see a correlation between the group velocity dispersion and the power conversion efficiency, partially confirmed by the

simulation reported in Fig. S2d-f. The coupling with the auxiliary cavity does not display a significant correlation with the comb efficiency, while the intrinsic linewidth shows that the least efficient combs also display higher intrinsic loss. Overall, the simulation analysis predicts that the photonic molecule microcomb is resilient to variations of the parameters considered in this study. Note however, that the simulation does not capture all physical features of the resonator, such as wavelength-dependent linewidth, which may be the reason for some of the measured combs exhibiting less than 40% efficiency.

The repetition rate changes across the wafer with a standard deviation of just 20 MHz (see Fig. S1b). Comparing these results with the thickness map (Fig. 2(a)) suggests that the repetition rate can be corrected by modifying the radius of the ring based on the chip position on the wafer. This could potentially lead to hundreds of devices in individual chips with repetition rate difference in the order of 10 MHz, a crucial aspect for dual-comb spectroscopy, comb synchronization [48], and advanced coherent communication systems [49] relying on phase-coherent transmitter and receiver combs with repetition rate differences within a few MHz.

5. Phase-sensitive tri-comb interferometry

The high yield of power-efficient solitons presents unique opportunities for chip-integrated applications such as spectroscopy [23] and range measurement [50–52]. Moreover, the generation of frequency combs through a photonic molecule configuration provides deterministic generation, stable operation [47], and a relatively flat spectral distribution. As proof of concept, we demonstrate how these capabilities can be used together.

In our demonstration, we propose a multi-comb interferometry scheme that enables parallel sampling of multiple devices under test. Based on multi-heterodyne detection, we employed a single local oscillator for the characterization of amplitude and phase in a sequential manner of two samples. This demonstration requires an exquisite control of the split resonance location and pump wavelength, and a small repetition rate variation across samples to downconvert the optical spectrum within the detection bandwidth of 5 GHz.

The experimental setup is illustrated in Fig. 4(a). We utilize three power-efficient combs: one for implementing the optical sampling (local oscillator) and the other two (comb A and comb B) are employed for consecutive measurements with the samples. The generation of coherent photonic molecule microcombs follows the same approach described in the Supplement 1. To establish mutual coherence, we employ the same pump laser at a wavelength of 1562.3 nm. The two combs were coupled to an optical pulse shaper [38,53] to simulate multiple different samples by adding a phase profile to the transmitted signal. The combs were combined with the local oscillator to obtain the interferograms reported in Fig. 4(b). The period corresponds to the difference in repetition rate between the local oscillator and the probe combs, which are ~ 15 ns ($1/\Delta f_{rep1}$) and ~ 58 ns ($1/\Delta f_{rep2}$) for comb A and B, respectively. The electro-optic down-converted repetition rate of the solitons is shown in Fig. 4(c), where Δf_{rep1} is 61.35 MHz and Δf_{rep2} is 17.23 MHz. Importantly, the laser pump generating the combs is not filtered out before detection. This is aided by the high conversion efficiency, which drastically reduces the intensity of the pump in the transmitted spectrum, hence allowing a simpler detection scheme.

The time-domain signal is processed using Fourier analysis to retrieve the spectral information, where an RF comb spaced by $\Delta f_{rep1,2}$ is obtained. The post-processing of the signal was implemented using coherent averaging and monitoring the drift of $\Delta f_{rep1,2}$ [50]. The number of beat notes is limited by the bandwidth of the optical filter programmed in the pulse shaper, which covers 45 nm. Figures 4(d) and (e) show the spectral phase information retrieved using the two solitons in consecutive measurements. These results were obtained when the pulse shaper was programmed for quadratic and cubic phase profiles. The first phase filter is the same for both combs A and B, and a different second filter is encoded in each comb. The empty circles

represent the retrieved spectral phase at the peaks of the RF combs and the lines are the functions programmed.

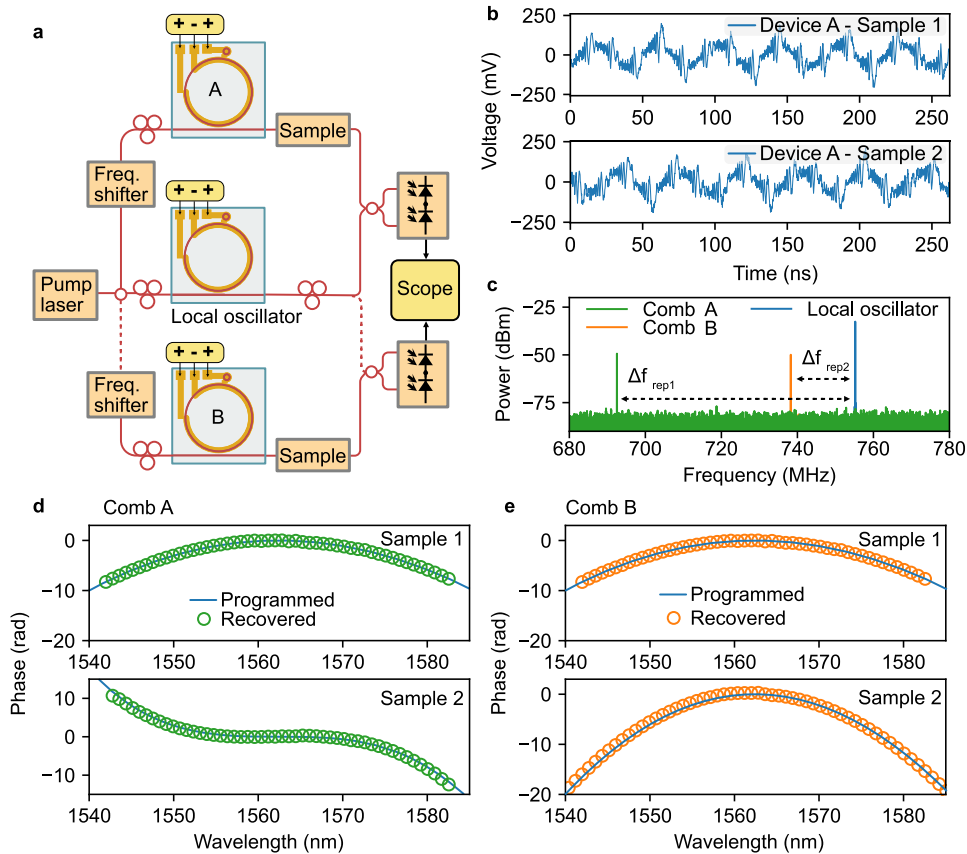


Fig. 4. Tri-comb interferometry. (a) Schematic of the experimental setup for the microcomb interferometry. (b) Interferogram traces of the beating between comb A and the local oscillator acquired with the of comb A with the two samples. (c) Downconverted beat notes of the local oscillator (blue), comb A (green), and comb B (orange). (d), (e) Plots of the programmed phase (solid line) and the recovered phase (empty dots).

The spectral resolution in our demonstration is ultimately limited by the linewidth of the individual comb tooth, similar to the dual-comb configuration [54]. The mode linewidth in a low-noise state microcomb is inherited from the linewidth of the pump laser [55], typically in the order of kHz. On the other hand, the spectral sampling is limited by the repetition rate of the microcomb which is 99.7 GHz in this case. The spectral sampling can be reduced to the MHz order which is appealing for stringent spectroscopy requirements by using a spectral interleaving approach [56] or by tuning the microcombs over a complete FSR [55]. The standard deviation of the residuals between the retrieved and the encoded phase is 0.07 rad for the first filter and 0.25 rad for the second filter, illustrating that the technique can recover with high spectral sensitivity multiple probe samples derived from a single continuous-wave laser.

6. Conclusion and outlook

In conclusion, we have reported the first statistical analysis of wafer-level manufacturing of chip-scale frequency comb generators. We have demonstrated 98% yield with microcombs

displaying a power conversion efficiency $>50\%$. These results are enabled by advances in ultra-low-loss silicon nitride processing and photonic-molecule engineering. The manufacturing process is subtractive and compatible with large-scale foundries [11]. When combined with heterogeneous integration of pump laser modules [22], these results pave the way for mass-market applications of chip-scale microcomb modules, such as datacenter interconnects in co-package optics or autonomous driving. Furthermore, the ability to reproduce with high fidelity nearly identical copies of high-performance microcombs might enable new modalities of sensing and spectroscopy that benefit from the economics of scale provided by silicon photonics.

Funding. European Research Council (CoG 771410, PoC 101064463); Vetenskapsrådet (2020-00453); Stiftelsen för Strategisk Forskning (FID 16-0011); Knut och Alice Wallenbergs Stiftelse (KAW 2018.0090); HORIZON EUROPE European Innovation Council (101158577).

Disclosures. M.G., O.B.H., and V.T.C. are co-founders of Iloomina AB. Others declare no conflicts of interest.

Data availability. The raw data used to produce the plots can be accessed at [57].

Supplemental document. See [Supplement 1](#) for supporting content.

References

1. S. Y. Siew, B. Li, F. Gao, *et al.*, “Review of Silicon Photonics Technology and Platform Development,” *J. Lightwave Technol.* **39**(13), 4374–4389 (2021).
2. C. Xiang, W. Jin, and J. E. Bowers, “Silicon nitride passive and active photonic integrated circuits: trends and prospects,” *Photonics Res.* **10**(6), A82 (2022).
3. W. Bogaerts, D. Pérez, J. Capmany, *et al.*, “Programmable photonic circuits,” *Nature* **586**(7828), 207–216 (2020).
4. A. A. Jørgensen, D. Kong, M. R. Henriksen, *et al.*, “Petabit-per-second data transmission using a chip-scale microcomb ring resonator source,” *Nat. Photonics* **16**(11), 798–802 (2022).
5. A. Rizzo, A. Novick, V. Gopal, *et al.*, “Massively scalable Kerr comb-driven silicon photonic link,” *Nat. Photonics* **17**(9), 781–790 (2023).
6. F. J. Ferraro, P. De Heyn, M. Kim, *et al.*, “Imec silicon photonics platforms: performance overview and roadmap,” *Next-Gen. Opt. Commun.: Components, Sub-Systems, Systems XII* G. Li, K. Nakajima, and A. K. Srivastava, eds., Vol. 12429, 9 (2023).
7. C. Sun, M. T. Wade, Y. Lee, *et al.*, “Single-chip microprocessor that communicates directly using light,” *Nature* **528**(7583), 534–538 (2015).
8. C. Rogers, A. Y. Piggott, D. J. Thomson, *et al.*, “A universal 3D imaging sensor on a silicon photonics platform,” *Nature* **590**(7845), 256–261 (2021).
9. A. Martin, D. Dodane, L. Leviandier, *et al.*, “Photonic integrated circuit-based FMCW coherent LiDAR,” *J. Lightwave Technol.* **36**(19), 4640–4645 (2018).
10. R. Chen, H. Shu, B. Shen, *et al.*, “Breaking the temporal and frequency congestion of LiDAR by parallel chaos,” *Nat. Photonics* **17**(4), 306–314 (2023).
11. A. Rahim, J. Goyvaerts, B. Szelag, *et al.*, “Open-Access Silicon Photonics Platforms in Europe,” *IEEE J. Sel. Top. Quantum Electron.* **25**(5), 1–18 (2019).
12. C. Gunn, A. Narasimha, B. Analui, *et al.*, “A 40Gb silicon photonics transceiver,” *Silicon Photonics II* J. A. Kubby and G. T. Reed, eds., Vol. 6477, 64770N (2007).
13. J. F. Bauters, M. J. R. Heck, D. John, *et al.*, “Ultra-low-loss high-aspect-ratio Si_3N_4 waveguides,” *Opt. Express* **19**(4), 3163 (2011).
14. J. Liu, G. Huang, R. N. Wang, *et al.*, “High-yield, wafer-scale fabrication of ultralow-loss, dispersion-engineered silicon nitride photonic circuits,” *Nat. Commun.* **12**(1), 2236 (2021).
15. V. Snigirev, A. Riedhauser, G. Lihachev, *et al.*, “Ultrafast tunable lasers using lithium niobate integrated photonics,” *Nature* **615**(7952), 411–417 (2023).
16. D. Zhu, L. Shao, M. Yu, *et al.*, “Integrated photonics on thin-film lithium niobate,” *Adv. Opt. Photonics* **13**(2), 242–352 (2021).
17. S. Arafin and L. A. Coldren, “Advanced InP Photonic Integrated Circuits for Communication and Sensing,” *IEEE J. Sel. Top. Quantum Electron.* **24**(1), 1–12 (2018).
18. P. Mu noz, P. W. L. van Dijk, D. Geuzebroek, *et al.*, “Foundry Developments Toward Silicon Nitride Photonics from Visible to the Mid-Infrared,” *IEEE J. Sel. Top. Quantum Electron.* **25**(5), 1–13 (2019).
19. Z. Ye, H. Jia, Z. Huang, *et al.*, “Foundry manufacturing of tight-confinement, dispersion-engineered, ultralow-loss silicon nitride photonic integrated circuits,” *Photonics Res.* **11**(4), 558 (2023).
20. C. Xiang, J. Guo, W. Jin, *et al.*, “High-performance lasers for fully integrated silicon nitride photonics,” *Nat. Commun.* **12**(1), 6650 (2021).
21. G. Roelkens, J. Zhang, L. Bogaert, *et al.*, “Micro-Transfer Printing for Heterogeneous Si Photonic Integrated Circuits,” *IEEE J. Sel. Top. Quantum Electron.* **29**(3: Photon. Elec. Co-Inte. and Ad), 1–14 (2023).
22. C. Xiang, W. Jin, O. Terra, *et al.*, “3D integration enables ultralow-noise isolator-free lasers in silicon photonics,” *Nature* **620**(7972), 78–85 (2023).

23. A. Dutt, C. Joshi, X. Ji, *et al.*, “On-chip dual-comb source for spectroscopy,” *Sci. Adv.* **4**(3), e1701858 (2018).
24. P. Marin-Palomo, J. N. Kemal, M. Karpov, *et al.*, “Microresonator-based solitons for massively parallel coherent optical communications,” *Nature* **546**(7657), 274–279 (2017).
25. H. Shu, L. Chang, Y. Tao, *et al.*, “Microcomb-driven silicon photonic systems,” *Nature* **605**(7910), 457–463 (2022).
26. T. J. Kippenberg, A. L. Gaeta, M. Lipson, *et al.*, “Dissipative Kerr solitons in optical microresonators,” *Science* **361**(6402), eaan8083 (2018).
27. Y. Sun, J. Wu, M. Tan, *et al.*, “Applications of optical microcombs,” *Adv. Opt. Photonics* **15**(1), 86 (2023).
28. A. Hermans, K. Van Gasse, and B. Kuyken, “On-chip optical comb sources,” *APL Photonics* **7**(10), 100901 (2022).
29. Y. Hu, M. Yu, B. Buscaino, *et al.*, “High-efficiency and broadband on-chip electro-optic frequency comb generators,” *Nat. Photonics* **16**(10), 679–685 (2022).
30. D. R. Carlson, D. D. Hickstein, W. Zhang, *et al.*, “Ultrafast electro-optic light with subcycle control,” *Science* **361**(6409), 1358–1363 (2018).
31. X. Xue, P.-H. Wang, Y. Xuan, *et al.*, “Microresonator Kerr frequency combs with high conversion efficiency,” *Laser Photonics Rev.* **11**(1), 1600276 (2017).
32. J. Li, C. Bao, Q.-X. Ji, *et al.*, “Efficiency of pulse pumped soliton microcombs,” *Optica* **9**(2), 231–239 (2022).
33. J. M. Chavez Boggio, D. Bodenmüller, S. Ahmed, *et al.*, “Efficient Kerr soliton comb generation in micro-resonator with interferometric back-coupling,” *Nat. Commun.* **13**(1), 1292 (2022).
34. Ó. B. Helgason, F. R. Arteaga-Sierra, Z. Ye, *et al.*, “Dissipative solitons in photonic molecules,” *Nat. Photonics* **15**(4), 305–310 (2021).
35. Ó. B. Helgason, M. Girardi, Z. Ye, *et al.*, “Surpassing the nonlinear conversion efficiency of soliton microcombs,” *Nat. Photonics* **17**(11), 992–999 (2023).
36. W. Jin, Q.-F. Yang, L. Chang, *et al.*, “Hertz-linewidth semiconductor lasers using CMOS-ready ultra-high-Q microresonators,” *Nat. Photonics* **15**(5), 346–353 (2021).
37. V. Torres-Company, J. Schröder, A. Fülöp, *et al.*, “Laser Frequency Combs for Coherent Optical Communications,” *J. Lightwave Technol.* **37**(7), 1663–1670 (2019).
38. V. Durán, S. Tainta, and V. Torres-Company, “Ultrafast electrooptic dual-comb interferometry,” *Opt. Express* **23**(23), 30557 (2015).
39. L. Chang, S. Liu, and J. E. Bowers, “Integrated optical frequency comb technologies,” *Nat. Photonics* **16**(2), 95–108 (2022).
40. K. Luke, A. Dutt, C. B. Poitras, *et al.*, “Overcoming Si₃N₄ film stress limitations for high quality factor ring resonators,” *Opt. Express* **21**(19), 22829 (2013).
41. R. M. Grootes, M. Dijkstra, Y. Klaver, *et al.*, “Crack barriers for thick SiN using dicing,” *Opt. Express* **30**(10), 16725 (2022).
42. K. H. Nam, I. H. Park, and S. H. Ko, “Patterning by controlled cracking,” *Nature* **485**(7397), 221–224 (2012).
43. M. H. P. Pfeiffer, C. Herkommer, J. Liu, *et al.*, “Photonic damascene process for low-loss, high-confinement silicon nitride waveguides,” *IEEE J. Sel. Top. Quantum Electron.* **24**(4), 1–11 (2018).
44. K. Wu and A. W. Poon, “Stress-released Si₃N₄ fabrication process for dispersion-engineered integrated silicon photonics,” *Opt. Express* **28**(12), 17708 (2020).
45. J. Gumpfer, W. Bather, and D. Wedel, “LPCVD silicon nitride uniformity improvement using adaptive real-time temperature control,” *IEEE Trans. Semicond. Manuf.* **16**(1), 26–35 (2003).
46. K. Twayana, Z. Ye, Ó. B. Helgason, *et al.*, “Frequency-comb-calibrated swept-wavelength interferometry,” *Opt. Express* **29**(15), 24363 (2021).
47. I. Rebolledo-Salgado, Ó. B. Helgason, V. Durán, *et al.*, “Active feedback stabilization of super-efficient microcombs in photonic molecules,” *Opt. Lett.* **49**(9), 2325 (2024).
48. B. Y. Kim, J. K. Jang, Y. Okawachi, *et al.*, “Synchronization of nonsoliton Kerr combs,” *Sci. Adv.* **7**(43), eabi4362 (2021).
49. Y. Geng, H. Zhou, X. Han, *et al.*, “Coherent optical communications using coherence-cloned Kerr soliton microcombs,” *Nat. Commun.* **13**(1), 1070 (2022).
50. P. Trocha, M. Karpov, D. Ganin, *et al.*, “Ultrafast optical ranging using microresonator soliton frequency combs,” *Science* **359**(6378), 887–891 (2018).
51. M. G. Suh and K. J. Vahala, “Soliton microcomb range measurement,” *Science* **359**(6378), 884–887 (2018).
52. J. Riemensberger, A. Lukashchuk, M. Karpov, *et al.*, “Massively parallel coherent laser ranging using a soliton microcomb,” *Nature* **581**(7807), 164–170 (2020).
53. D. E. Leaird, F. Ferdous, A. M. Weiner, *et al.*, “Dual-comb electric-field cross-correlation technique for optical arbitrary waveform characterization,” *Opt. Lett.* **34**(24), 3875–3877 (2009).
54. I. Coddington, N. Newbury, and W. Swann, “Dual-comb spectroscopy,” *Optica* **3**(4), 414–426 (2016).
55. P. Del’Haye, T. Herr, E. Gavartin, *et al.*, “Octave spanning tunable frequency comb from a microresonator,” *Phys. Rev. Lett.* **107**(6), 063901 (2011).
56. C. Bao, Z. Yuan, L. Wu, *et al.*, “Architecture for microcomb-based GHz-mid-infrared dual-comb spectroscopy,” *Nat. Commun.* **12**(1), 6573 (2021).
57. M. Girardi, Ó. B. Helgason, C. H. López-Ortega, *et al.*, “Data accompanying Superefficient microcombs at the wafer level,” Zenodo (2025), <https://doi.org/10.5281/zenodo.15363056>.